

# Electromagnetically induced transparency with hybrid silicon-plasmonic traveling-wave resonators

Dimitra A. Ketzaki,<sup>a)</sup> Odysseas Tsilipakos, Traianos V. Yioultsis, and Emmanouil E. Kriezis  
*Department of Electrical and Computer Engineering, Aristotle University of Thessaloniki,  
 Thessaloniki GR-54124, Greece*

(Received 9 July 2013; accepted 3 September 2013; published online 19 September 2013)

Spectral filtering and electromagnetically induced transparency (EIT) with hybrid silicon-plasmonic traveling-wave resonators are theoretically investigated. The rigorous three-dimensional vector finite element method simulations are complemented with temporal coupled mode theory. We show that ring and disk resonators with sub-micron radii can efficiently filter the lightwave with minimal insertion loss and high quality factors ( $Q$ ). It is shown that disk resonators feature reduced radiation losses and are thus advantageous. They exhibit unloaded quality factors as high as 1000 in the telecom spectral range, resulting in all-pass filtering components with sharp resonances. By cascading two slightly detuned resonators and providing an additional route for resonator interaction (i.e., a second bus waveguide), a response reminiscent of EIT is observed. The EIT transmission peak can be shaped by means of resonator detuning and interelement separation. Importantly, the respective  $Q$  can become higher than that of the single-resonator structure. Thus, the possibility of exploiting this peak in switching applications relying on the thermo-optic effect is, finally, assessed.  
 © 2013 AIP Publishing LLC. [<http://dx.doi.org/10.1063/1.4821796>]

## I. INTRODUCTION

Hybrid plasmonic waveguides (HPWs) have recently drawn considerable attention due to the favorable compromise between mode confinement and propagation loss they offer.<sup>1,2</sup> More specifically, such waveguides confine the optical field inside a low-index dielectric gap, formed between a high-index semiconductor and a metallic region. Through an advantageous synergy of “plasmonic” and index-contrast guiding mechanisms, they allow for nanoscale mode confinement and, at the same time, reduced propagation loss, outperforming other plasmonic waveguides. Characteristic of the tight mode confinement they offer is the ability of forming bent waveguide structures with sub-micron radii. As a result, they constitute a prime candidate for realizing integrated plasmonic components comprising traveling-wave resonators with nanoscale footprint and high quality factors.<sup>3–8</sup>

Among the HPW variants proposed thus far, the conductor-gap-silicon (CGS) waveguide<sup>9,10</sup> offers some distinct advantages. Specifically, it is technologically simple, being a layered planar structure based on the mature silicon on insulator (SOI) technology. More importantly, it is compatible with standard SOI waveguides, meaning that light can be coupled in and out of CGS-based components with minimal insertion loss through silicon photonic access waveguides.<sup>10</sup> The CGS waveguide has been employed in the implementation of a broad range of passive components including waveguide bends,<sup>10</sup> splitters,<sup>10,11</sup> polarizers,<sup>12</sup> couplers,<sup>13</sup> and resonators.<sup>5,6</sup>

In this work, we focus on elaborate wavelength-selective components employing CGS-based traveling-wave resonators. First, the performance characteristics of all-pass filtering structures comprising either ring or disk resonators

side-coupled to a bus waveguide are thoroughly examined. Subsequently, two detuned resonators are employed in a cascaded configuration for the purpose of demonstrating components featuring a response reminiscent of electromagnetically induced transparency (EIT), i.e., featuring a sharp transmission peak inside a broad absorption dip. The investigation of photonic analogs of EIT is already a familiar concept in plasmonics. So far, mainly standing-wave resonators have been utilized for the task.<sup>14–17</sup> However, traveling-wave resonators can also be used for this purpose. Indeed, an EIT-like response has been obtained using two detuned traveling-wave resonators in Ref. 18. Due to the lossy resonators employed, however, the produced EIT peak does not possess high-quality-factor values. Our aim is to design a structure featuring a sharp EIT peak and subsequently exploit this peak in switching applications. To this end, we employ CGS-based high-quality-factor resonators and adopt a configuration already successfully demonstrated in silicon photonics.<sup>19</sup> Finally, we assess the possibility of utilizing the thermo-optic effect for tuning the structure response.

The paper is organized as follows: In Sec. II the guiding characteristics of the underlying CGS waveguide are presented. Section III investigates CGS-based all-pass filtering structures comprising ring, disk, and donut-shaped resonators. The combination of two slightly detuned CGS-based resonators in order to produce an EIT-like response is assessed in Sec. IV. Section V addresses the tuning capabilities of these structures by means of the thermo-optic effect. Finally, in Sec. VI, a brief summary and the concluding remarks are provided.

## II. CONDUCTOR-GAP-SILICON WAVEGUIDE

The CGS waveguide cross-section is depicted in Fig. 1(a). It consists of a low-index  $\text{SiO}_2$  region ( $n_{\text{SiO}_2} = 1.45$ )

<sup>a)</sup>dketzaki@auth.gr

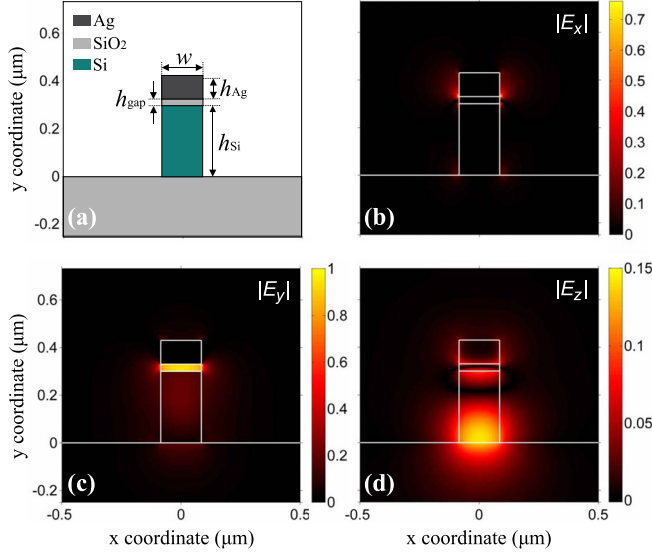


FIG. 1. (a) Cross-section of the CGS waveguide. Geometrical parameters:  $w = 170$  nm,  $h_{\text{Si}} = 300$  nm,  $h_{\text{gap}} = 30$  nm,  $h_{\text{Ag}} = 100$  nm. Material properties:  $n_{\text{Si}} = 3.48$ ,  $n_{\text{SiO}_2} = 1.45$ ,  $n_{\text{Ag}} = 0.14 - j11.4$ . (b)–(d) Distributions of electric field components for the fundamental TM-like mode at a working wavelength of  $1.55 \mu\text{m}$ . Note that the dominant electric field component ( $E_y$ ) is confined inside the silica layer, whereas the axial component ( $E_z$ ) resides mainly in the silicon region.

sandwiched between a high-index Si layer ( $n_{\text{Si}} = 3.48$ ) and a silver cap ( $n_{\text{Ag}} = 0.14 - j11.4$  (Ref. 20)). The combined three-layer guiding region resides on a silica substrate. We choose the geometrical parameters in such a way so that a tightly confined mode with a high propagation length is supported. Specifically, the exact values are as follows:  $w = 170$  nm,  $h_{\text{Si}} = 300$  nm,  $h_{\text{gap}} = 30$  nm, and  $h_{\text{Ag}} = 100$  nm.

A finite-element-based mode solver is employed for solving the 2D eigenvalue problem of the waveguide cross-section. The effective refractive index obtained at  $1550$  nm is  $2.034 - j0.002$ . The imaginary part corresponds to a propagation length  $L_{\text{prop}}$  (the  $e$ -folding distance of the optical intensity) of  $60 \mu\text{m}$ . At the same time, the effective mode area, calculated through  $A_{\text{eff}} \triangleq (\iint |\mathbf{E}|^2 dx dy)^2 / \iint |\mathbf{E}|^4 dx dy$ , is  $0.0217 \mu\text{m}^2$ , indicating sub-wavelength confinement and verifying that the considered waveguide can indeed provide a favorable balance between mode confinement and propagation loss. The distributions of all three electric field components are depicted in Figs. 1(b)–1(d), normalized relative to the maximum value of  $|E_y|$ , which is the dominant component (TM-like mode). Clearly, the  $E_y$  component is strongly confined inside the silica gap [Fig. 1(c)]. However, the axial component ( $E_z$ ) resides inside the Si region [Fig. 1(d)], something that will prove useful for thermo-optically controlling the waveguide characteristics in Sec. V, given the high thermo-optic coefficient of silicon.

### III. RESONATOR FILTERING STRUCTURES

In this section we examine the characteristics of CGS-based traveling-wave resonators. Both ring and disk resonators are considered, and a comparison between them is provided. Their filtering performance in simple all-pass configurations (resonator side-coupled to a single bus waveguide) is also

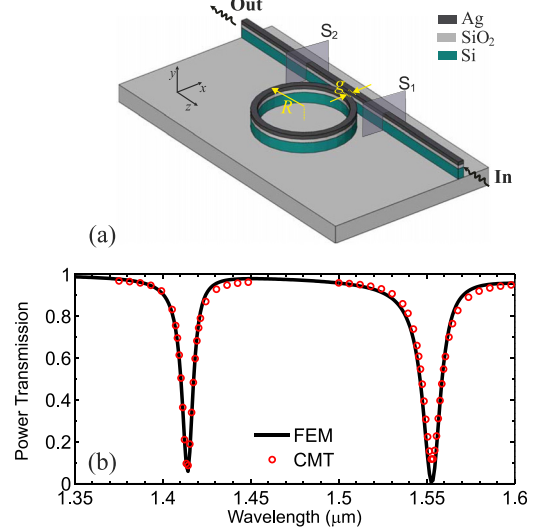


FIG. 2. (a) Microring resonator filtering geometry with geometrical parameters  $R = 0.93 \mu\text{m}$ ,  $g = 120$  nm. (b) Power transmission calculated between reference input and output ports versus wavelength. The solid line represents FEM simulation results whereas circles stand for the CMT-based response.

assessed, whereas a donut-based resonator filtering structure is investigated, as well.

### A. Sub-micron ring resonator filters

The first structure under investigation is an all-pass filter composed of a bus CGS waveguide side-coupled with a sub-micron ring resonator [Fig. 2(a)]. We begin with the eigenvalue analysis of the uncoupled microring, since it is expected to provide a first indication concerning the modes supported by the resonator and their respective characteristics. For the numerical analysis, the three-dimensional vector finite element method (3D-VFEM)<sup>21–23</sup> is utilized. The computational domain is discretized using triangular prism (edge) elements, while absorbing boundary conditions (ABCs) are implemented on all sides of the bounding box.

The eigenvalue analysis has been conducted keeping the resonator footprint sub-micron ( $R = 0.93 \mu\text{m}$ ) and setting the remaining geometrical parameters exactly as those given in Fig. 1(a). The supported modes are listed in Table I. Three modes can be distinguished with intrinsic quality factors ( $Q_i$ ) and azimuthal mode numbers that increase as the resonance wavelength decreases. In particular, in the wavelength region of interest (around  $1550$  nm) a  $7$ th azimuthal-order mode is supported. Its resonance wavelength is  $1556$  nm, and a quality factor of  $355$  is attained. This quality factor is associated with two loss mechanisms: resistive losses in the metallic layer and radiation losses standing for the power leakage from the resonator. The corresponding quality factors  $Q_{\text{res}}$

TABLE I. Microring resonator eigenvalue analysis. Azimuthal mode numbers and quality factors for three resonances of a  $R = 0.93 \mu\text{m}$  microring.

Wavelength (nm)	Azimuthal mode number	Intrinsic quality factor ( $Q_i$ )
1418	8	675
1556	7	355
1743	6	175

and  $Q_{\text{rad}}$ , for this mode specifically (at 1556 nm) are  $Q_{\text{res}}=730$  and  $Q_{\text{rad}}=690$ , signifying that the two mechanisms equally contribute to the overall loss of the ring resonator. The relatively high intrinsic quality factors indicate that the ring resonator is a good candidate for filtering applications.

Such a filtering component is investigated next. In this configuration the sub-micron resonator is side-coupled to a single CGS waveguide by a coupling gap  $g$  measured between the edges of the two [Fig. 2(a)]. The 3D-VFEM is utilized again for the numerical analysis. A two-dimensional eigenvalue problem is first solved on the waveguide cross section, in order to obtain the supported hybrid mode and use it as excitation on the input port. Since the fundamental mode supported by the CGS waveguide is a hybrid one, the ABCs concerning the input and output ports are modified in order to account for the coordinate-dependent wave impedance.<sup>24</sup> On all the remaining boundaries of the computational box, ordinary first-order ABCs are implemented. The power transmission is computed, by calculating the guided power which propagates through a reference output plane (denoted by  $S_2$  in Fig. 2(a)) and normalizing it with respect to the power level computed on a reference input plane (denoted by  $S_1$ ). The spacing between the two reference planes is  $2R$ . We should note here that this power transmission is associated only with the power carried by the quasi-TM plasmonic SiO<sub>2</sub> mode. This has been verified through the computation of an overlap integral involving the field distribution on the waveguide output plane.

Figure 2(b) depicts the transmission spectrum for a microring-based resonator filter with structural parameters  $R=0.93\ \mu\text{m}$  and  $g=120\ \text{nm}$ . The coupling gap value has been chosen for critically coupling resonator and waveguide. In a wavelength range of 1.35–1.6  $\mu\text{m}$  two resonances can be distinguished, associated with the resonator modes of 8<sup>th</sup> and 7<sup>th</sup> azimuthal mode order (at 1414 nm and 1553 nm, respectively). For both resonances, the loaded quality factors (extracted from the transmission curve through  $f_{\text{res}}/\delta f$ ) exhibit values over 120. Their decrease as compared with the unloaded eigenvalue problem solved earlier is attributed to the extra loss mechanism that exists in this case and is associated with the coupling between the ring and the bus waveguide. The free spectral range (FSR) is approximately 140 nm, whereas minimal insertion loss (IL < 0.2 dB) is attained, signifying the structure capability for efficient lightwave filtering. The geometrical parameters chosen in designing the waveguide (Sec. II) ensure that critical coupling can be achieved for technologically feasible gap values (over 100 nm) and that no higher-order modes are excited in the resonator which would lead to mode beating at the output waveguide.

The finite element method (FEM)-based simulation process, from which the filter response has been obtained, can significantly increase the computational demands even for the configuration of a simple filtering model as the one examined earlier. A first estimation of this filter transmission spectrum could be obtained through the calculation of a response based on temporal coupled mode theory (CMT).<sup>25</sup> The CMT-based equation that we use in order to verify this fact is of the form

$$\frac{d\alpha(t)}{dt} = j\omega_l\alpha(t) - \frac{1}{\tau_l}\alpha(t) - j|\kappa|s_i, \quad (1)$$

where  $s_i$  is the waveguide mode amplitude of the incident wave,  $|\alpha(t)|^2$  represents the energy stored in the ring resonator,  $|\kappa|$  is the coupling coefficient, and  $\omega_l$ ,  $1/\tau_l$  are the resonance frequency regarding the loaded resonator and its decay rate, respectively.

In order to obtain the necessary parameters for feeding the above equation, apart from the eigenvalue analysis of the isolated ring structure (unloaded eigenvalue problem), an additional eigenvalue problem concerning the ring resonator in the presence of a CGS waveguide (loaded eigenvalue problem) is solved, as well. The intrinsic ( $Q_i$ ) and loaded quality factors ( $Q_l$ ) are extracted from the uncoupled and coupled eigenvalue problems, respectively, whereas the quality factor associated with the coupling loss mechanism ( $Q_{\text{wg}}$ ) can be calculated through

$$\frac{1}{Q_{\text{wg}}} = \frac{1}{Q_l} - \frac{1}{Q_i}. \quad (2)$$

Therefore, the resonance frequency,  $\omega_l$ , can be obtained directly from the loaded eigenvalue problem, while the value of  $1/\tau_l$  is calculated through  $Q_l$ . The coupling coefficient,  $|\kappa|$ , is obtained through the relationship  $|\kappa| = \sqrt{2/\tau_{\text{wg}}}$ , with  $1/\tau_{\text{wg}}$  being the energy decay rate due to the coupling loss mechanism and thus obtained through  $Q_{\text{wg}}$ . The CMT-based power transmission, computed between the input and output reference ports, can be seen in Fig. 2(b). The response based on CMT corresponds very well with that extracted from the FEM simulation process, giving a clear indication of the transmission spectrum. Therefore, an estimation of the structure resonance behavior can be obtained before the time consuming FEM-based harmonic analysis is conducted, providing the necessary design guidelines. This could be considered particularly useful for the investigation of more complicated structures.

Subsequently, the propagation analysis results are compared with those extracted from the eigenvalue problem in order to check their agreement. The comparison between the two eigenvalue analyses and the propagation problem, for both resonances (around 1415 nm and 1550 nm), can be seen in Table II. Comparing, at first, the results obtained from the

TABLE II. Comparison between propagation and eigenvalue analysis for a microring resonator filter with parameters  $R=0.93\ \mu\text{m}$ ,  $g=120\ \text{nm}$ .

		Eigenvalue analysis (uncoupled) <sup>a</sup>	Eigenvalue analysis (coupled) <sup>a</sup>	Propagation problem
$m=7^{\text{b}}$	$\lambda_{\text{res}}$ (nm)	1556	1554	1553
	Q factor	355	128	129
$m=8^{\text{b}}$	$\lambda_{\text{res}}$ (nm)	1418	1414	1414
	Q factor	675	187	193

<sup>a</sup>Uncoupled eigenvalue analysis refers to the single ring resonator problem whereas the coupled one refers to the problem of a ring resonator in the presence of a bus waveguide.

<sup>b</sup> $m$  stands for the azimuthal mode number.

two eigenvalue problems, we can observe that in the presence of the bus waveguide the resonance wavelengths are slightly reduced (coupling-induced resonance frequency shift (CIFS)),<sup>26</sup> whereas the quality factors decrease due to coupling. The quality factors associated with this loss mechanism,  $Q_{wg}$ , for the modes of 7th and 8th azimuthal order are approximately 200 and 260. At the same time, the results obtained from the loaded eigenvalue problem appear to be in very good agreement with those extracted from the harmonic analysis.

## B. Sub-micron disk resonator filters

In this section, we focus on disk resonator filters, an alternative to microring resonator filters studied in Sec. III A. Due to the absence of an inner boundary, we expect the disk resonator to exhibit lower radiation losses and therefore higher intrinsic quality factors.<sup>27</sup> At the same time, the possible excitation of higher radial order modes could lead to a spectrum with various transmission dips for the associated filtering structure.

We begin again with the eigenvalue analysis of the uncoupled disk resonator, in order to detect the supported modes and assess their characteristics. The ring radius is set to a sub-micron value of  $0.85 \mu\text{m}$ , and modes are sought in the telecom wavelength range  $1.4\text{--}1.65 \mu\text{m}$ . Six modes can be distinguished exhibiting azimuthal and radial mode order that are given in Table III. The intrinsic quality factors associated with each mode are also listed in Table III. Obviously, the microdisk structure can support first (modes 1 and 4) or second-radial-order plasmonic modes (modes 2 and 6), as anticipated for a disk resonator. The quality factors, regarding the plasmonic modes of interest (of first radial order), approach in this case 1000 for wavelengths around  $1550 \text{ nm}$  and are significantly higher than those obtained with the ring resonator structure.

The mode profiles for all the supported modes, listed in Table III, are depicted in Fig. 3. More specifically, it is the real part of  $E_y$  that is plotted on the  $xz$ -plane corresponding to the electric field maximum (silica region mid-plane for modes 1, 2, 4, 6 and silicon region mid-plane for modes 3, 5). Both the azimuthal and the radial mode order are observed. What is interesting, however, is that apart from these modes, which are mainly located in the  $\text{SiO}_2$  layer, there are also others that are mostly confined in the Si region

TABLE III. Microdisk resonator eigenvalue analysis. Azimuthal and radial mode numbers and quality factors for six resonances of a  $R=0.85 \mu\text{m}$  microdisk.

	Resonance wavelength (nm)	Azimuthal mode number	Radial mode number	Quality factor
1	1422	8	1	1700
2	1448	5	2	186
3 <sup>a</sup>	1464	7	1	1650
4	1564	7	1	920
5 <sup>a</sup>	1599	6	1	615
6	1614	4	2	105

<sup>a</sup>Modes mostly confined in the Si region.

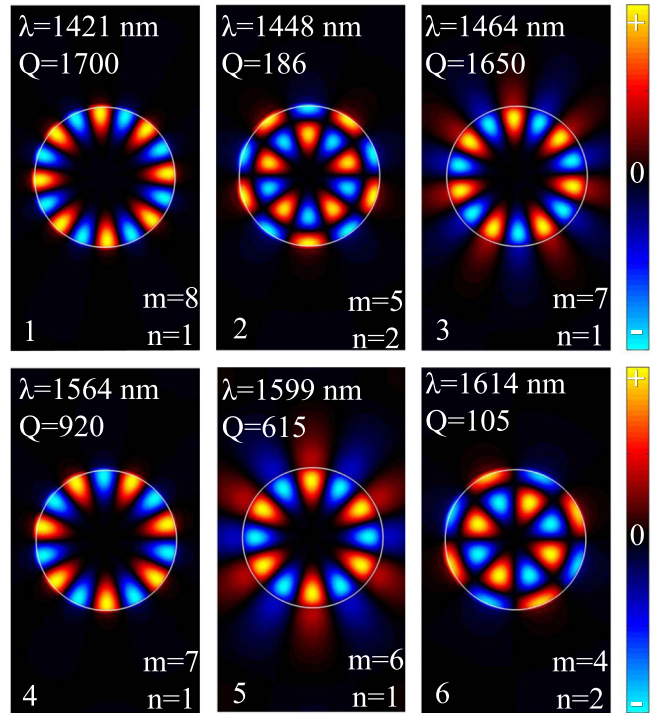


FIG. 3. Real part of the  $E_y$  component for the six disk resonator modes in the wavelength range  $1.4\text{--}1.65 \mu\text{m}$ . Modes 1, 2, 4, and 6 are plotted on the  $xz$  mid-plane in the  $\text{SiO}_2$  layer, whereas modes 3 and 5 are depicted on the Si layer mid-plane, where they exhibit their respective maxima.

(modes 3 and 5). This can be confirmed by plotting the electric field intensity  $|\mathbf{E}|^2$  on vertical  $xy$ -planes (Fig. 4), where the distinction between the plasmonic modes, 4 and 6, of first and second radial order, respectively, and the photonic mode, 5, can be easily verified. Supposing, therefore, that in a filtering configuration which includes a disk resonator, all these supported modes are going to be excited, a transmission spectrum with several resonance dips is expected to develop.

The disk resonator filter is investigated next. A schematic of the simulated structure is depicted in Fig. 5(a). The geometrical parameters are  $R=0.85 \mu\text{m}$  and  $g=150 \text{ nm}$ . A FEM simulation analysis has been conducted resulting in the power transmission response shown in Fig. 5(c) (solid line). Several transmission dips can be observed, each one associated with a mode of the resonator (Fig. 3). In particular, the two main resonance dips, appearing at  $1418 \text{ nm}$  and  $1562 \text{ nm}$ , are due to the excitation of plasmonic modes of first radial order and exhibit (loaded) quality factors in the order of 300. On the other hand, the minor resonances that

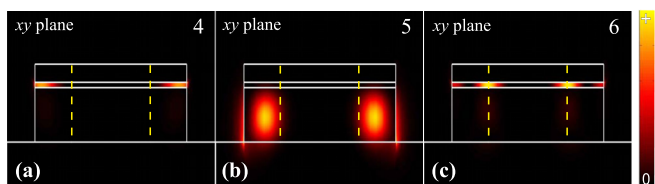


FIG. 4.  $|\mathbf{E}|^2$  on a vertical  $xy$ -plane for modes 4, 5, and 6. (a) Plasmonic mode of first radial order, (b) Si-located mode, and (c) plasmonic mode of second radial order. Dashed lines represent the inner boundary of the proposed donut structure.

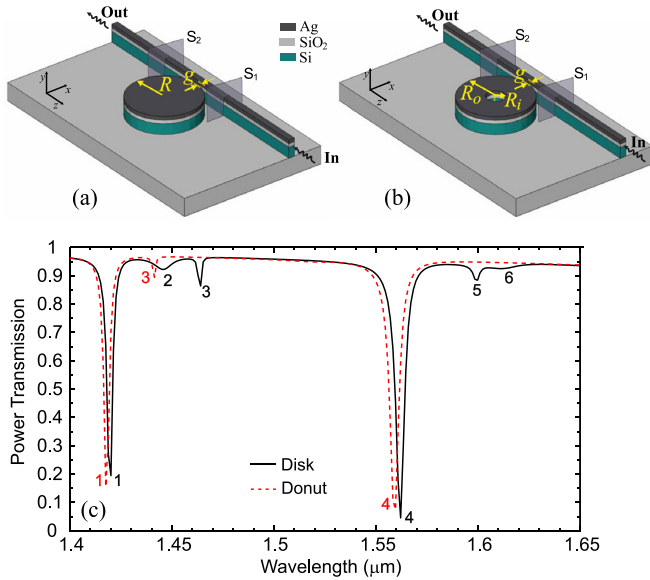


FIG. 5. (a) Microdisk filtering structure with disk radius  $R=0.85\ \mu\text{m}$  and  $g=150\ \text{nm}$ . (b) Donut filtering structure with  $R_o=0.85\ \mu\text{m}$ ,  $R_i=0.45\ \mu\text{m}$ , and  $g=150\ \text{nm}$ . (c) Power transmission between input and output port for both disk-resonator (solid line) and donut-resonator (dashed line) filters. Note the suppression of secondary transmission dips corresponding to second radial order plasmonic and Si-located modes.

can be observed are related either with the plasmonic modes of second radial order or the modes located in the Si region. These secondary transmission dips are not only shallow but also far away from the primary resonances. As a result, they do not have a deleterious impact on filter performance. If we wish to obtain a cleaner transmission spectrum, however, we can replace the disk with a donut resonator [Fig. 5(b)]. The inner boundary of the donut ( $R_i$ ) can be properly selected so as to suppress the second-radial-order plasmonic modes (modes 2 and 6 in Fig. 3), without affecting the first-order plasmonic modes of interest (modes 1 and 4 in Fig. 3). Thus, the  $R_i$  value is chosen by considering the electric field distribution of the supported modes. Specifically, it is set to  $R_i=0.45\ \mu\text{m}$ , noted with dashed lines in Fig. 4. All remaining geometrical parameters are kept exactly the same as in the disk structure.

The donut-based filter response can be seen in Fig. 5(c) (dashed line). Clearly, the second-radial-order modes have been eliminated from the transmission spectrum, while the main transmission dips due to the plasmonic modes of first radial order have remained almost unimpaired. We should note here that there is a minor resonance remaining close to the first transmission dip (1418 nm) even for the donut-based filtering configuration, which is due to the excitation of a Si-located mode. In any case, in the telecom spectral range (around 1550 nm) the donut resonator can offer a clean resonance behavior.

#### IV. ELECTROMAGNETICALLY INDUCED TRANSPARENCY WITH TWO TRAVELING-WAVE RESONATORS

Having assessed the performance of CGS-based traveling wave resonators, we focus on more elaborate structures

comprising two such resonators, capable of exhibiting EIT-like response. Our aim is to produce a sharp EIT peak possessing a higher quality factor than those of the transmission dips for the all-pass filtering structures (Sec. III) and subsequently exploit this peak in switching applications. For this purpose, we employ two slightly detuned resonators in a configuration already successfully demonstrated in silicon photonics.<sup>19</sup> More specifically, the two resonators are side coupled to a bus waveguide (separated by a center-to-center distance  $s$ ) and an additional route for resonator interaction is provided, i.e., a second access waveguide [Fig. 6(a)]. By adjusting the spacing  $s$  and the resonator detuning, we can shape the structure response and modify the peak characteristics.

Compared to silicon photonics, the device can be much more compact. More specifically, the ring resonators employed in Ref. 19 possess radii in the order of  $5\ \mu\text{m}$ . It is the tight confinement of hybrid plasmonic waveguides that permits resonator radii in the order of  $1\ \mu\text{m}$ , like the ones employed in this work, offering a significant reduction in device footprint. This, for example, is demonstrated in Ref. 10 where the bending losses of CGS and standard SOI waveguides are compared. The CGS waveguide clearly outperforms silicon-based ones for bending radii  $<1\ \mu\text{m}$ . Although CGS waveguides are accompanied by resistive losses, the performance is not significantly impaired since the resonator separation is kept small and the quality factors of the individual resonators are relatively high. Finally, an additional advantage of the CGS-based device is that the

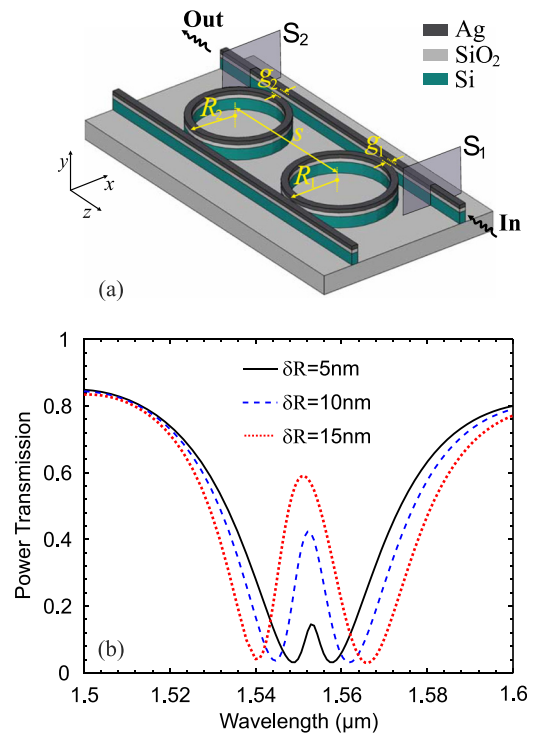


FIG. 6. (a) EIT structure involving two detuned microring resonators.  $R_{1,2} = R_0 \pm \delta R$  with  $R_0 = 1.3\ \mu\text{m}$ ,  $g_0 = 120\ \text{nm}$ , and  $s = 3.81\ \mu\text{m}$  ( $m=5$ ). (b) Power transmission between input and output port for three detuning scenarios. For  $\delta R = 5, 10,$  and  $15\ \text{nm}$  the quality factors of the transmission peaks are 345, 165, and 100, whereas the extinction ratio is 6.6, 11.5, and 13 dB, respectively.

metallic circuitry already present for guiding the plasmonic mode can be utilized for carrying a control signal, as well. This unique feature of plasmonic waveguides can be exploited for thermo-optically tuning the structure response, a possibility explored in Sec. V.

We first analyze the configuration comprising two detuned microring resonators [Fig. 6(a)]. Since  $R_{1,2}$  are modified around a central radius,  $R_0 = 1.3 \mu\text{m}$ , with  $R_{1,2} = R_0 \pm \delta R$ , the gaps,  $g_1$  and  $g_2$ , between the bus waveguides and each resonator become  $g_1 = g_0 - \delta R$  and  $g_2 = g_0 + \delta R$ , respectively, where  $g_0$  is the central gap distance value. Given the resonator spacing, the phase accumulated between the two resonators is  $\phi = \omega n_{\text{eff}} s / c$ , where  $\omega$  is the operating frequency. When the interelement distance is chosen to be a multiple of the guide wavelength ( $s = m\lambda_g$ ) the phase between the rings becomes  $\phi = m2\pi$  and the EIT peak is anticipated to be symmetric.<sup>14</sup> Indeed, the 3D-VFEM transmission curves of Fig. 6(b) indicate just that. For three different detuning scenarios and an interelement distance value  $s = 3.81 \mu\text{m}$  ( $m = 5$ ), symmetric transmission peaks can be observed in the region between individual ring resonances. Quality factors greater than those taken from the single resonator configuration can be produced (345, 165, and 100 for  $\delta R = 5, 10$ , and  $15 \text{ nm}$ , respectively), showing the capability of obtaining narrow spectral widths without significantly affecting structure compactness. Apparently, the resonator detuning influences the spectral response providing higher quality factors ( $Q$ ) as the parameter  $\delta R$  decreases. This happens, however, at the cost of the extinction ratio (ER) between the EIT peak and the lower power transmission value, which is smaller for the sharper peaks (6.6, 11.5, and  $13 \text{ dB}$  for  $\delta R = 5, 10$ , and  $15 \text{ nm}$ , respectively). Such a trade-off between  $Q$  and ER is justified by the fact that the coupling to the waveguides is not the only decay pathway for the resonators energy. Since other decay mechanisms are also present (radiation or resistive losses) the detuning does not allow for unity peak transmission and arbitrarily spectral widths at the same time.

In Fig. 7, a parametric analysis with respect to coupling gap and resonator separation is presented. Specifically, Fig. 7(a) depicts the influence of the coupling gap on the transmission spectrum. Choosing one detuning scenario ( $\delta R = 10 \text{ nm}$ ), we modify the gap (120 nm) to larger and smaller values. As we can see, for narrower gaps higher  $Q$  values can be attained whereas the extinction ratio becomes smaller, showing that the decrease in ER due to the detuning radius reduction in Fig. 6(b) could be possibly compensated

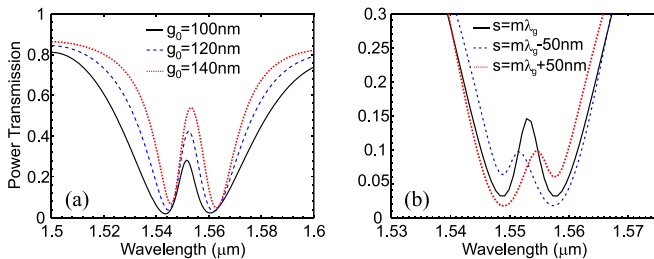


FIG. 7. Parametric investigation for the microring EIT structure ( $s = m\lambda_g$  with  $m = 5$  throughout). (a) Power transmission for various gap values ( $\delta R = 10 \text{ nm}$ ). (b) Power transmission for mismatched interelement spacings ( $\delta R = 5 \text{ nm}$ ).

by a small gap modification. Fig. 7(b) investigates the effect of the interelement spacing on structure response ( $\delta R = 5 \text{ nm}$ ). Clearly, when the separation  $s$  is not an integer multiple of the guide wavelength the EIT peak is asymmetric, shifting to lower or higher wavelengths. This asymmetry has a deleterious effect on peak quality, as both  $Q$  and ER decrease.

As in the case of the filtering components analyzed previously (Sec. III), we can have a fairly accurate picture of the spectral response for the EIT-structure under investigation using temporal CMT. In order to calculate the CMT-based transmission response, we form the following equation system:

$$\frac{d\alpha_1(t)}{dt} = j\omega_1\alpha_1(t) - \frac{1}{\tau_1}\alpha_1(t) - j|\kappa_1|s_{1i} - j|\kappa_1|s_{1r}, \quad (3a)$$

$$\frac{d\alpha_2(t)}{dt} = j\omega_2\alpha_2(t) - \frac{1}{\tau_2}\alpha_2(t) - j|\kappa_2|s_{2i}, \quad (3b)$$

based on the schematic of the model shown in Fig. 8(a). The waveguide mode amplitudes are related to the energy stored in the resonators through

$$s_{2i} = e^{-j\phi} s_{1r} = e^{-j\phi} [s_{1i} - j|\kappa_1|\alpha_1(t)], \quad (4a)$$

$$s_{1r} = e^{-j\phi} [-j|\kappa_2|\alpha_2(t)]. \quad (4b)$$

Four eigenvalue problems are solved to feed the CMT equations, corresponding to the loaded and unloaded case of each resonator. An auxiliary eigenvalue analysis regarding the CGS waveguide is also performed in order to record the dispersion relation  $n_{\text{eff}}(\lambda)$ . The reason of such an analysis is twofold; it is primarily necessary for calculating the phase shift,  $\phi$ , between the two ring resonators through  $\phi = \omega n_{\text{eff}} s / c$ , taking into account the dispersion of  $n_{\text{eff}}(\lambda)$  and secondarily for specifying the loss along the separation distance  $s$  in order to adjust the CMT result to the input-output port spacing ( $R_1 + s + R_2$ ) by imposing the corresponding propagation loss. This way, we can perform a fair comparison between the rigorous 3D-VFEM transmission curve and CMT results (Fig. 8(b)). Clearly, the agreement between the two responses is very good, signifying the capability to use CMT as a prototyping tool for the investigation of such complex structures, as well.

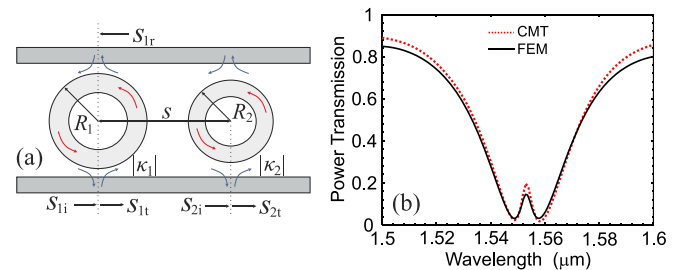


FIG. 8. (a) Schematic of the two-ring configuration used as model for the CMT equation system. The waveguide mode amplitudes related to the energy stored in the resonators are noted with  $s_{i,r}$  for each ring,  $|\kappa_{1,2}|$  are the coupling coefficients associated with each ring, whereas  $R_{1,2}$  are the resonator radii. (b) Comparison between FEM response and response extracted by temporal CMT for detuning  $\delta R = 5 \text{ nm}$ .

Since disk resonator structures can provide resonances with higher  $Q$  values (Sec. III B), we change the rings with disk resonators forming a structure as the one shown in Fig. 9(a). We choose geometrical parameters following the design guidelines obtained from Sec. III B. The spacing,  $s$ , between the two resonators is chosen again as a multiple of the guide wavelength  $s = 2.3 \mu\text{m}$  ( $m = 3$ ), whereas their radii are slightly detuned around  $R_0 = 0.85 \mu\text{m}$ . Fig. 9(b) depicts the FEM-simulated transmission spectrum of the microdisk-based structure for three different detuning scenarios:  $\delta R = 3, 5,$  and  $7 \text{ nm}$ . Since the resonance wavelengths of the disk configuration are more sensitive in radius changes than those of the ring structure, the detuning distances are now smaller. This can be justified by the fact that due to the absence of the inner boundary the disk modes reside closer to the resonator center.<sup>27</sup> The effective radius is, thus, smaller and consequently smaller radius variations can induce larger changes in resonant frequency. Obviously, a transparency peak clearly forms in the region between individual disk resonances, even for  $\pm 3 \text{ nm}$  radius variation. The peak quality factors are significantly greater in this case (390, 195, and 125, respectively), and the extinction ratios approach or even exceed 10 dB for all the three cases (9.4, 11.8, and 12.9 dB for  $\delta R = 3, 5,$  and  $7 \text{ nm}$ ). For the  $\delta R = 3 \text{ nm}$  case the transmission minimum observed around 1556 nm is only 4 nm far from the transparency peak. A further investigation of this fact and its relation to possible switching applications is presented in Sec. V.

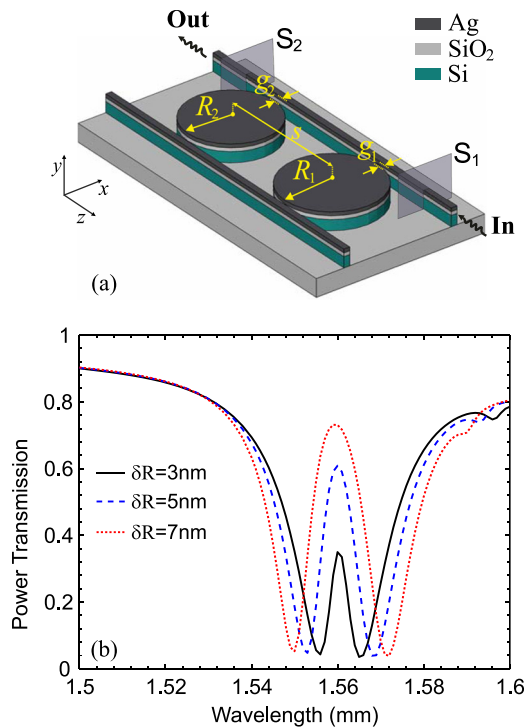


FIG. 9. (a) Microdisk EIT structure.  $R_{1,2} = R_0 \pm \delta R$  with  $R_0 = 0.85 \mu\text{m}$ ,  $g_1 = g_0 - \delta R$ , and  $g_2 = g_0 + \delta R$  with  $g_0 = 120 \text{ nm}$ . (b) FEM-simulated power transmission between input and output port for three radius detuning scenarios. For  $\delta R = 3, 5,$  and  $7 \text{ nm}$  the quality factors of the transmission peaks are 390, 195, and 125, whereas the extinction ratio is 9.4, 11.8, and 12.9 dB, respectively.

We should note here that in the upper limit of our spectral region a small transmission recession can be observed for all the three detuning scenarios. This faint drop can be attributed to a second-radial-order disk mode that has been probably excited and we have already investigated in Sec. III (see Fig. 5(c)). Around the wavelength region of interest, however, the transmission spectrum is clean, allowing the safe extraction of the EIT peak characteristics.

## V. THERMO-OPTIC TUNING

The EIT structures presented in Sec. IV provide sharp transparency peaks with quality factors exceeding those obtained with the single-resonator filters. In this section, we explore the possibility of exploiting these peaks in switching applications. More specifically, we employ the thermo-optic effect in order to alter the resonant frequencies of the resonators involved and thus tune the structure response. Since resonator structures are particularly sensitive to phase changes, this can lead to efficient switching, as demonstrated with other plasmonic waveguides.<sup>28,29</sup>

We examine the disk-based structure of Sec. IV for a radius variation  $\delta R = 3 \text{ nm}$  [Fig. 9]. As we have already mentioned, the first transmission minimum for this case is observed at a wavelength that is only 4 nm away from the transparency peak. This means that if the transmission curve is shifted by 4 nm a transmission maximum will appear in the place of the transmission minimum. In other words, the component will change state. Given the high thermo-optic coefficient of silicon<sup>30</sup> ( $1.8 \times 10^{-4} \text{ K}^{-1}$ ), the required wavelength shift can be provided by heating the structure. We assume that the whole structure is uniformly heated and take into account the thermo-optic coefficient of  $\text{SiO}_2$ ,<sup>30</sup> though much smaller, as well ( $1 \times 10^{-5} \text{ K}^{-1}$ ). A modest temperature change of  $\delta T = 60 \text{ K}$ , which leads to a refractive index change for Si  $\delta n = 0.011$ , is sufficient for obtaining the required shift, as indicated by Fig. 10, where the corresponding FEM-simulated transmission curves are depicted. The extinction ratio between the two states is approximately 8 dB, verifying the tunability capabilities of the disk resonator structure and its potential use for the realization of switching components. Let us finally note that assuming a

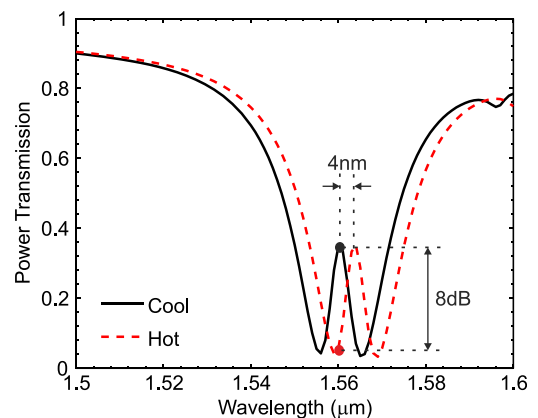


FIG. 10. Thermo-optic tuning for the structure depicted in Fig. 9(a). FEM simulated power transmission for heated and unheated states. The extinction ratio between the two states is 8 dB.

structure without resonator detuning and heating only one resonator in order to induce the EIT peak would require a temperature difference approximately three times higher to obtain a similar ER between states. Therefore, heating both detuned resonators is beneficial.

## VI. CONCLUSION

To summarize, CGS-based components utilizing sub-micron traveling-wave resonators have been analyzed by means of vectorial 3D-FEM simulations. Disk resonator structures exhibit advantageous characteristics for filtering applications as compared to ring resonators. The nature of the various modes supported by the disks has been investigated, and a donut-based configuration has been proposed so that a cleaner transmission spectrum can be obtained.

Two slightly detuned traveling-wave resonators have been utilized, next, to produce EIT-like peaks sharper than those provided by the single-resonator filtering structures. It has been confirmed that both the quality factor values and the symmetry of the produced EIT transmission peaks can be modified by adjusting the spacing between the two resonators. The possibility of utilizing temporal CMT as a prototyping tool for such responses has been also verified. Finally the perspective of exploiting these transparency peaks in switching applications has been investigated. Relying on the thermo-optic effect, the tuning capability of a microdisk-based EIT structure has been demonstrated, reflecting its potential use for the realization of compact switching components.

## ACKNOWLEDGMENTS

This research was co-financed by the European Union (European Social Fund–ESF) and Greek national funds through the Operational Program “Education and Lifelong Learning” of the National Strategic Reference Framework (NSRF). Research Funding Program: THALES (Project ANEMOS), Investing in knowledge society through the European Social Fund.

- <sup>1</sup>M. Z. Alam, J. Meier, J. S. Aitchison, and M. Mojahedi, in *CLEO/QELS*, paper JThD112 (2007).
- <sup>2</sup>R. F. Oulton, V. J. Sorger, D. A. Genov, D. F. P. Pile, and X. Zhang, *Nat. Photonics* **2**, 496 (2008).
- <sup>3</sup>R. Salvador, A. Martinez, C. Garcia-Meca, R. Ortuno, and J. Marti, *IEEE J. Sel. Top. Quantum Electron.* **14**, 1496 (2008).
- <sup>4</sup>X.-Y. Zhang, A. Hu, J. Z. Wen, T. Zhang, X.-J. Xue, Y. Zhou, and W. W. Duley, *Opt. Express* **18**, 18945 (2010).
- <sup>5</sup>Y. Song, J. Wang, M. Yan, and M. Qiu, *J. Opt.* **13**, 075001 (2011).
- <sup>6</sup>D. Dai, Y. Shi, S. He, L. Wosinski, and L. Thylen, *Opt. Express* **19**, 23671 (2011).
- <sup>7</sup>H.-S. Chu, Y. Akimov, P. Bai, and E.-P. Li, *Opt. Lett.* **37**, 4564 (2012).
- <sup>8</sup>S. Zhu, G. Q. Lo, and D. L. Kwong, *Opt. Express* **20**, 15232 (2012).
- <sup>9</sup>D. Dai and S. He, *Opt. Express* **17**, 16646 (2009).
- <sup>10</sup>M. Wu, Z. Han, and V. Van, *Opt. Express* **18**, 11728 (2010).
- <sup>11</sup>J. Wang, X. Guan, Y. He, Y. Shi, Z. Wang, S. He, P. Holmström, L. Wosinski, L. Thylen, and D. Dai, *Opt. Express* **19**, 838 (2011).
- <sup>12</sup>M. Z. Alam, J. S. Aitchison, and M. Mojahedi, *Opt. Lett.* **37**, 55 (2012).
- <sup>13</sup>Y. Song, J. Wang, M. Yan, and M. Qiu, *J. Opt.* **13**, 075002 (2011).
- <sup>14</sup>R. D. Kekatpure, E. S. Barnard, W. Cai, and M. L. Brongersma, *Phys. Rev. Lett.* **104**, 243902 (2010).
- <sup>15</sup>Z. Han and S. I. Bozhevolnyi, *Opt. Express* **19**, 3251 (2011).
- <sup>16</sup>H. Lu, X. Liu, D. Mao, Y. Gong, and G. Wang, *Opt. Lett.* **36**, 3233 (2011).
- <sup>17</sup>H. Lu, X. Liu, and D. Mao, *Phys. Rev. A* **85**, 053803 (2012).
- <sup>18</sup>Z. Han, C. E. Garcia-Ortiz, I. P. Radko, and S. I. Bozhevolnyi, *Opt. Lett.* **38**, 875 (2013).
- <sup>19</sup>Q. Xu, S. Sandhu, M. L. Povinelli, J. Shakya, S. Fan, and M. Lipson, *Phys. Rev. Lett.* **96**, 123901 (2006).
- <sup>20</sup>P. B. Johnson and R. W. Christy, *Phys. Rev. B* **6**, 4370 (1972).
- <sup>21</sup>J. Jin, *The Finite Element Method in Electromagnetics* (Wiley, New York, 2002).
- <sup>22</sup>D. I. Karatzidis, T. V. Yioultsis, and E. E. Kriezis, *J. Lightwave Technol.* **26**, 2002 (2008).
- <sup>23</sup>O. Tsilipakos, A. Ptilakis, A. C. Tasolamprou, T. V. Yioultsis, and E. E. Kriezis, *Opt. Quantum Electron.* **42**, 541 (2011).
- <sup>24</sup>O. Tsilipakos, E. E. Kriezis, and T. V. Yioultsis, *Microwave Opt. Technol. Lett.* **53**, 2626 (2011).
- <sup>25</sup>H. A. Haus, *Waves and Fields in Optoelectronics* (Prentice-Hall, New Jersey, 1984).
- <sup>26</sup>O. Tsilipakos, T. V. Yioultsis, and E. E. Kriezis, *J. Appl. Phys.* **106**, 093109 (2009).
- <sup>27</sup>O. Tsilipakos and E. E. Kriezis, *Opt. Commun.* **283**, 3095 (2010).
- <sup>28</sup>O. Tsilipakos, E. E. Kriezis, and S. I. Bozhevolnyi, *J. Appl. Phys.* **109**, 073111 (2011).
- <sup>29</sup>K. Hassan, J.-C. Weeber, L. Markey, and A. Dereux, *J. Appl. Phys.* **110**, 023106 (2011).
- <sup>30</sup>M. W. Geis, S. J. Spector, R. C. Williamson, and T. M. Lyszczarz, *IEEE Photon. Technol. Lett.* **16**, 2514 (2004).